The Conducting Spin-Crossover Compound Combining Fe(II) Cation Complex with TCNQ in a Fractional Reduction State

Yuri N. Shvachko,*,[†] Denis V. Starichenko,*,[†] Aleksander V. Korolyov,[†] Eduard B. Yagubskii,*,[‡] Alexander I. Kotov,[‡] Lev I. Buravov,[‡] Konstantin A. Lyssenko,[§] Vladimir N. Zverev,[∥,⊥] Sergey V. Simonov,[∥] Leokadiya V. Zorina,[∥] Olga G. Shakirova,[#] and Lyudmila G. Lavrenova[g]

[†]M. N. Miheev Institute of Metal Physics, Ural Branch of Russian Academy of Sciences, S. Kovalevskaya Street 18, Yekaterinburg 620137, Russia

[‡]Institute of Problems of Chemical Physics, Russian Academy of Sciences, Semenov Avenue 1, Chernogolovka, 142432 Moscow District, Russia

[§]A.N. Nesmeyanov Institute of Organoelement Compounds, Russian Academy of Sciences, Vavilov Street 28, Moscow 119991, Russia

[∥]Institute of Solid State Physics, Russian Academy of Sciences, Ossipyan Street 2, Chernogolovka 142432, Moscow District, Russia

[⊥]Moscow Institute of Physics and Technology, Dolgoprudnyi, Moscow District 141700, Russia

[#]Komsomolsk-on-Amur State Technical University, Lenin Avenue 27, Komsomolsk-on-Amur 681013, Russia

[g]Nikolaev Institute of Inorganic Chemistry, Siberian Branch of Russian Academy of Sciences, Lavrentyev Avenue 3, Novosibirsk 630090, Russia

S *Supporting Information*

ABSTRACT: The radical anion salt $[Fe\{HC(pz)_3\}_2]$-$(TCNQ)_3$ demonstrates conductivity and spin-crossover (SCO) transition associated with Fe(II) complex cation subsystem. It was synthesized and structurally characterized at temperatures 100, 300, 400, and 450 K. The compound demonstrates unusual for 7,7,8,8-tetracyanoquinodimethane (TCNQ)-based salts quasi-two-dimensional conductivity. Pronounced changes of the in-plane direct-current resistivity and intensity of the electron paramagnetic resonance (EPR) signal, originated from TCNQ subsystem, precede the SCO transition at the midpoint $T^* = 445$ K. The boltzmannian growth of the total magnetic response and structural changes in the vicinity of T^* uniquely show that half $[Fe\{HC(pz)_3\}_2]$ cations exist in high-spin state. Robust broadening of the EPR signal triggered by the SCO transition is interpreted in terms of cross relaxation between the TCNQ and Fe(II) spin subsystems.
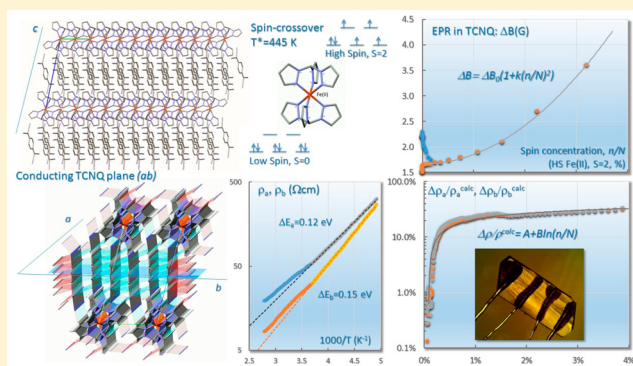
INTRODUCTION

Molecular materials, in which conductivity and magnetism cooperate in the same crystal lattice, attract attention, because their synergy may lead to novel physical phenomena.[1] So far, the basic class of such materials was mainly represented by the quasi-two-dimensional (super)conductors based on the radical cation salts of bis(ethylenedithio)tetrathiafulvalene and its derivatives with paramagnetic metal complex anions of different nature.[1b−f] It is of a considerable interest to use the octahedral cation complexes of Fe(II) and Fe(III), showing reversible spin-crossover (SCO) between high-spin (HS) and low-spin (LS) states of the metal ion, as a magnetic subsystem in combination with an anion-conducting subsystem.[2] The conducting sublattice of such hybrid materials could be represented by the radical anion subsystem based on $[M(dmit)_2]^{\bullet\delta-}$ complexes (M = Ni, Pd, Pt; dmit = 4,5-

dithiolato-1,3-dithiole-2-thione; $0 < \delta < 1)^3$ and/or 7,7,8,8,-tetracyanoquinodimethane $((TCNQ)^{\bullet\delta-}, 0 < \delta < 1)^4$ in a fractional oxidation or reduction state, respectively. The SCO induced by temperature, pressure, or light irradiation is accompanied by the changes in the coordination environment of the metal ion.[5] The electrical conductivity of most molecular conductors is very sensitive to external and/or chemical pressure.[6] There is every reason to believe that SCO transition would affect the conductivity at least via a chemical compression. Furthermore, magnetic interactions between the subsystems make possible a realization of a spin-dependent electronic transport. Several conducting SCO systems are known that combine the cation complexes of Fe(III) with
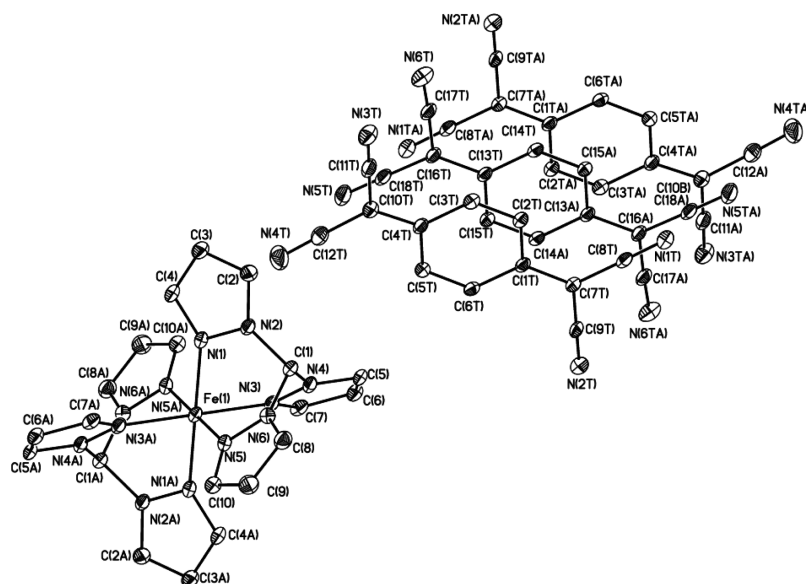
Figure 1. A formula unit of complex **I**. The $\{Fe[HC(pz)_3]_2\}^{2+}$ cation and one of the TCNQ molecules occupy the special position (the center of symmetry). All atoms with label **A** are obtained from the base ones by the symmetry operations (1) $-x, -y, -z$ for cation and (2) $-x + 1, -y + 2, -z + 1$ for TCNQ.

$[M(dmit)_2]^{\delta-}$ anions[7] and the only system containing $TCNQ^{\delta-}$ anion.[8] The interplay between SCO and conductivity was reported for two of them.[7e,f] Although the variations of the spin moment at SCO are the same for Fe(II) and Fe(III), $\Delta S = 2$, the average bond length for a given donor atom changes significantly greater in the case for Fe(II) ions ($\Delta r \approx 8-15\%$) rather than that for Fe(III) ions ($\Delta r \approx 5\%$). Besides Fe(II) complexes are diamagnetic in LS and paramagnetic in HS states. In this context, the Fe(II) complexes seem preferable for the design of conducting SCO systems. The synthesis of electroactive SCO systems based on redox-labile Fe(II) complexes with $[M(dmit)_2]^{\delta-}$ anions is most likely impossible, principally because of high oxidation potential of $[M(dmit)_2]^{-}$ to $[M(dmit)_2]^{0}$. Recently, Nihei et al. have proposed an alternative approach to design the conducting SCO compounds based on Fe(II) complexes: the ligands contain potentially conducting fragments such as tetrathiafulvalene (TTF) and its derivatives.[9] The SCO complex with the conductivity $\sigma_{rt} = 2.6 \times 10^{-3}$ Ω^{-1} cm^{-1} and coupling between transport properties and the spin transition was synthesized within this approach. The domain of the conducting TCNQ radical anion salts with SCO Fe(II) cation complex as counterion remains essentially unexplored. The only structurally characterized SCO Fe(II) complex with $TCNQ^{\bullet-}$ counterion, $[Fe(abpt)_2(TCNQ)_2]$, is known.[10] However, this complex is an insulator ($\sigma_{rt} = 5 \times 10^{-10}$ Ω^{-1} cm^{-1}).[10b] Dielectric properties are associated primarily with strong dimerization of TCNQ radicals and absence of long-range stacking. More recently the materials $[Fe^{II}(tpma)(xbim)](X)(TCNQ)_{1.5}\cdot DMF$ (X = ClO_4, BF_4 and DMF = dimethylformamide), $[Co^{II}(terpy)_2](TCNQ)_3\cdot CH_3CN$, and $[Co^{II}(pyterpy)_2](TCNQ)_2$ showing SCO and electrical conductivity have been obtained.[11] Here, the first three compounds have a relatively high conductivity ($\sigma_{rt} \approx 2 \times 10^{-1}$ Ω^{-1} cm^{-1}) and coexist with a partially reduced $TCNQ^{\bullet\delta-}$ radical ($\delta = 0.67$), whereas the latter compound reveals low conductivity ($\sigma_{rt} = 5 \times 10^{-6}$ Ω^{-1} cm^{-1}) and coexists with a fully reduced $TCNQ^{\bullet 1-}$ radical.

In this paper, we report synthesis, structure, and physical properties of the new conducting SCO compound based on the

Fe(II) cationic complex with TCNQ counterion in a fraction reduction state, $[Fe\{HC(pz)_3\}_2](TCNQ)_3$ (**I**), where $HC(pz)_3$ = tris(pyrazol-1-yl)methane. Pronounced changes of the in-plane direct-current (dc) resistivity and intensity of the EPR signal, originated from TCNQ subsystem, precede the SCO transition. Boltzmannian growth of the total magnetic response with the temperature as well as structural changes during the transition allows direct detection of the transformation from LS to HS state in $[Fe\{HC(pz)_3\}_2]$ cations. Robust broadening of the EPR signal triggered by the SCO transition is interpreted in terms of cross relaxation between the TCNQ and Fe(II) spin subsystems. The interactions between the conducting spin system and local moments of Fe(II) ions can possibly contribute to the observed effect.

RESULTS AND DISCUSSION

Synthesis and Structure. Black rhombic crystals of **I** were obtained in argon atmosphere by spontaneous crystallization from solution containing $[Fe\{HC(pz)_3\}_2]I_2\cdot H_2O$[12] and TCNQ (see Experimental). The synthesis was based on ability of a neutral TCNQ molecule to be reduced by an iodide ion to a radical anion.[4a] Thermal analysis of **I** has shown that the complex is stable up to 200 °C. The differential scanning calorimetry (DSC) curve reveals the exothermal peaks at 256.5 and 272.1 °C, associated with decomposition of the complex. As this takes place, the ions with m/e 26 (CN) are observed in the mass spectrum (Supporting Information, Figure S1).

X-ray structural analysis was performed at 100, 300, 400, and 450 K. Compound **I** crystallizes in the triclinic space group $P\bar{1}$ ($Z = 1$, $Z' = 0.5$) with three TCNQ molecules per one $[Fe\{HC(pz)_3\}_2]^{2+}$ complex cation (Figure 1). The cation and one of the TCNQ molecules occupy special positions, that is, center of symmetry, so there are only two independent TCNQ molecules, further denoted as **A** (one in the general position) and **B** (one at the center of symmetry). The overall crystal structure of **I** can be described as that consisting of cationic and anionic layers parallel to the crystallographic plane ab (Figure 2).
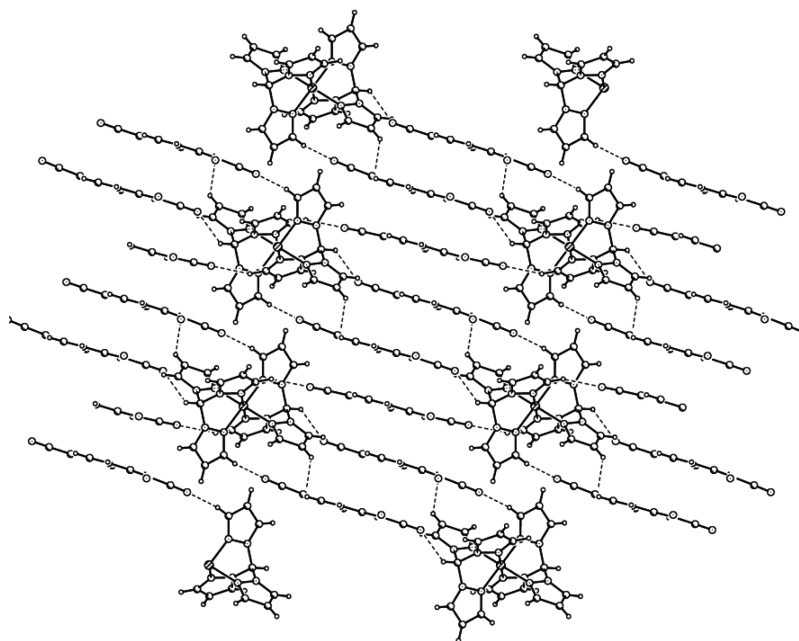
Figure 2. Fragment of the crystal packing in **I** showing alternate cationic and anionic layers (view along *a*). Interlayer C−H···N contacts (2.41−2.70 Å) between cations and anions are shown by dashed lines.

The crystal structure details are further described for the 100 K structure. In the $[Fe\{HC(pz)_3\}_2]$, the Fe(II) ion at 100 K must be in an LS state, judging by the average Fe−N bond length (1.968(5) Å; Supporting Information, Figure S2 and Table S1). Indeed, the value of ca. 1.97 Å is typical for the LS octahedral Fe(II)N$_6$ complexes, whereas in an HS state of the Fe(II)N$_6$ complexes the average Fe−N bond distance is 2.17 Å.[13] All other parameters, including the average torsion angle Fe(1)−N−N−C (177.63°; Table S1), also coincide with the expected values for the LS state.[13b,c] The stacking-bonded cationic chains run along the crystallographic axis *a*, while the TCNQ anions are stacked along the [110] direction (Supporting Information, Figure S3). The cation···cation stacking interaction is observed between the independent pyrazole cycles (C···C contacts are 3.343(2) Å; Supporting Information, Figure S4). In the anionic stacks, centrosymmetric triads **A**···**B**···**A** are formed with a rather strong stacking interaction (Figure 3). At 100 K the interplane **A**···**B** separation is 3.04(2) Å, and the distance for the shortest C···C contacts varies in the range of 3.101(4)−3.328(2) Å. The above triads are linked by **A**···**A** stacking interactions (the interplane distance is 3.36(1) Å) mainly involving C(CN)$_2$ groups
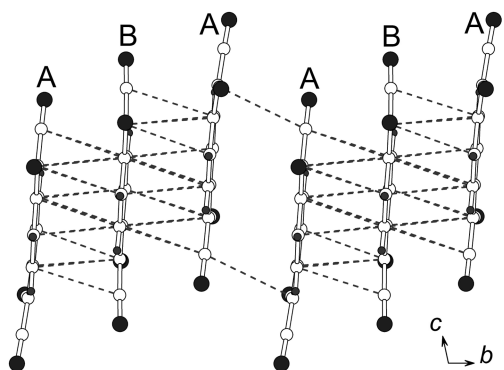
(Supporting Information, Figure S5). These stacks are assembled into layers by C···N interactions and weak side-by-side C−H···N−C hydrogen bonds (Supporting Information, Figures S6 and S7). Cation···anion interactions in **I** also include weak C−H···N contacts (Figure 2). The majority of these contacts belong to the molecule TCNQ (**B**). On the basis of the formula of **I**, the average charge on the TCNQ$^{\bullet\delta-}$ radical should be −0.67 or −2.0 on repeating **ABA** triad of the stack. It was shown that the charge state of TCNQ could be estimated from its bond distances.[14] There is a great deal of work relating the carbon−carbon bond lengths in TCNQ to the degree of charge (δ) held on it.[14a,b] By using the Kistenmacher relationship[14b−d] $\delta = A[c/(b + d)] + B$ ($A = -41.667$; $B = 19.833$; $b-d$ are the average bond lengths of TCNQ shown in Scheme of Table S2), we estimated the charge distribution for **A** and **B** TCNQ molecules in the stack (−0.5 and −0.89, respectively; Supporting Information, Table S2). These values point to different degrees of a charge acceptance by the TCNQ species in **I**. The total charge on the various TCNQ species is −1.89, which is in agreement with the +2 charge on the $[Fe\{HC(pz)_3\}_2]$ cation.

According to magnetic measurements, a transformation from LS to HS state in compound **I** begins above room temperature (see the next section). To follow the structural changes upon the SCO transition, X-ray single-crystal diffraction study was made at 300, 400, and 450 K. The last temperature is close to the maximum for our X-ray setup and is slightly below the temperature of decomposition of the complex (Supporting Information, Figure S1).

Structural changes in both cationic magnetic and anionic conducting subsystems were analyzed. It is found that Fe−N bond length values in the cation, which determine the spin state, are almost the same at 100, 300, and 400 K and become remarkably longer at 450 K (Tables 1 and S1). Taking into account average Fe−N bond lengths of 1.97 and 2.17 Å for LS and HS state of octahedral Fe(II)N$_6$ complexes, respectively,[13] we can conclude that SCO transition in **I** is at the beginning at

Figure 3. Stacking interactions in the anionic columns at 100 K.

Table 1. Average Fe−N Bond Length Values in [Fe{HC(pz)₃}₂](TCNQ)₃ (I), the Charges^a (δ) of Different TCNQ$^{•\delta-}$ Species A and B, and Intrastack A···B and A···A Separations at Different Temperatures

	100 K	300 K	400 K	450 K
(Fe−N)$_{av}$, Å	1.968(5)	1.965(5)	1.983(5)	2.050(7)
δ (A)	−0.53	−0.58	−0.60	−0.62
δ (B)	−0.94	−0.84	−0.80	−0.77
A···B, Å	3.04(2)	3.08(2)	3.12(2)	3.34(3)
A···A, Å	3.36(1)	3.38(1)	3.40(1)	3.38(1)

^{a}Estimated from Kistenmacher's empirical formula (Supporting Information, Table S2) and scaled to make the total charge on **ABA** triad exactly equal to −2.

400 K [(Fe−N)$_{av}$ distance of 1.983(5) Å], whereas temperature of 450 K and (Fe−N)$_{av}$ of 2.050(7) Å correspond to the middle of the transition with ∼40−50% of Fe(II) centers in HS state. Note, the HS and LS cations are statistically distributed within the crystal, since we have only one independent [Fe{HC-(pz)₃}₂]$^{2+}$ moiety in the unit cell.

Changes in the anionic subsystem versus temperature are more continuous. Charges on the TCNQ$^{•\delta-}$ **A** and **B** radicals calculated using the Kistenmacher formula are listed in Supporting Information, Table S2. The calculated values were scaled to make the total charge on TCNQ **ABA** triad exactly equal to −2 according to stoichiometry of the compound. The resulting scaled values are collected in Table 1. They demonstrate linear dependence from the temperature, visually illustrated in Figure 4. Clear charge disproportionation between
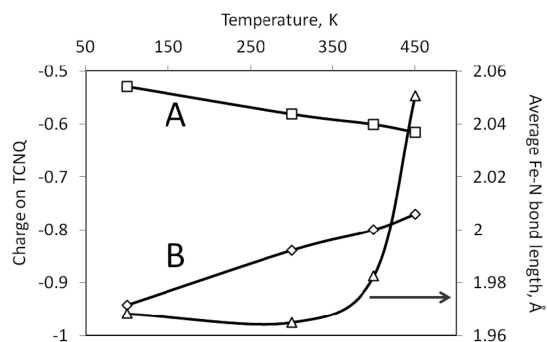

Figure 4. Temperature dependences of average Fe−N bond lengths as well as calculated and scaled TCNQ$^{•\delta-}$ charges. Note that decreasing of bond length values between 100 and 300 K is likely an artifact connected with errors in determination of unit cell parameters by different X-ray diffractometers.

two independent TCNQ$^{•\delta-}$ radicals observed at 100 K (with charges on **A** and **B** near −0.5 and −1, respectively) gradually vanished upon heating. The charge state of TCNQ$^{•\delta-}$ becomes more uniform and at 450 K reaches to −0.62 (**A**) and −0.77 (**B**); that is, it tends to the average −0.67 level. A comparison between the temperature dependences of **A** and **B** charges and average Fe−N bond length in Figure 4 leads to a conclusion that evolution of the TCNQ$^{•\delta-}$ charge is determined by temperature variation rather than by geometry of the neighboring Fe(II) cationic complexes. Similar charge evolution along the trimerized TCNQ$^{•\delta-}$ stacks with the temperature was earlier observed in TCNQ salts with diamagnetic organic cations, that is, in the absence of magnetic subsystem.[15] Contrary to the charge distribution, intrastack spacing between

adjacent TCNQ units demonstrates clear dependence on SCO transition (Table 1). At 100 K **A···B** interplane distance inside the triad is much shorter than **A···A** distance between the triads. Both of them demonstrate weak growth at temperatures below SCO; however, at 450 K **A···B** separation sharply increases following notable lengthening of average Fe−N bonds at SCO and becomes close to **A···A** separation, while the latter remains almost unchanged. The more uniform charge density distribution and the more regular interplanar spacing between the TCNQ units in HS state as compared to LS state was also observed in the conductive SCO complexes [Fe^{II}(tpma) (xbim)](X) (TCNQ)$_{1.5}$·DMF (X = ClO₄, BF₄) suggesting a greater electron delocalization in the HS state.[11a]

To confirm the structure of the polycrystalline sample **I**, X-ray powder diffraction (XRPD) was performed on the powdered dried sample, which was prepared by crushing the crystals. The XRPD pattern was compared with simulated pattern calculated from the single-crystal data for **I** (Supporting Information, Figure S8). The comparison confirmed the presence of a single phase in the bulk material.

Conductivity and Magnetic Properties. The normalized dc resistance, $R(T)/R(300\ K)$, measured by a standard four-probe method for the single crystal [Fe{HC-(pz)₃}₂]$^{2+}$(TCNQ)₃$^{2-}$, demonstrates a semiconducting type of behavior (Figure 5). The placement of the electrodes on the

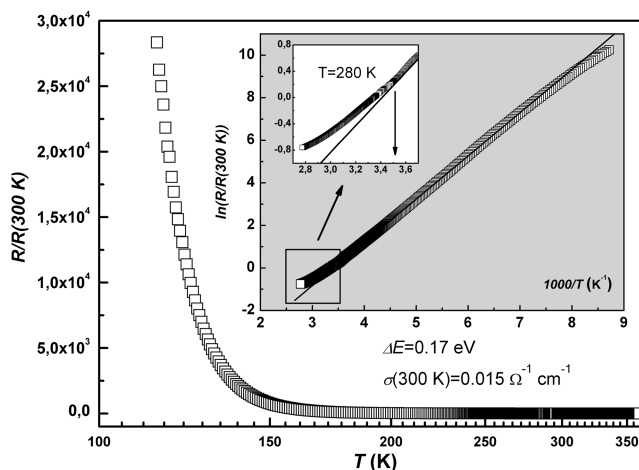**Figure 5.** Temperature dependence of the normalized resistance, $R(T)/R(300\ K)$. (inset) Logarithmic plot of the $R(T)/R(300\ K)$ vs scaled reciprocal temperature, $1000/T$. Solid line, $R_{calc}(T) = \exp(\Delta E/kT)$, with the energy gap $\Delta E = 0.17$ eV, is the best-fit ($R_{factor} = 0.99977$) of the experimental data in the range $120 < T < 250$ K. A deviation of the experimental data $R(T)$ from the theoretical curve $R_{calc}(T)$ at $T > 280$ K is shown in detail in the dilated window.

crystal is shown in Figure S9. The value of the conductivity at room temperature is $1.5 \times 10^{-2}\ \Omega^{-1}\ cm^{-1}$. Below 280 K the data points are well-described by the exponential law $R_{calc}(T) = \exp(\Delta E/kT)$ with the energy gap $\Delta E = 0.17$ eV (inset, Figure 5). The results of the Montgomery method measurements (see Experimental) above 200 K are presented in Figures 6 and 7 for the in-plane ($\rho_\parallel$) and out-of-plane ($\rho_\perp$) resistivity tensor components. The conductivity in the plane ab is practically isotropic ($\sigma_{\parallel TCNQ\ stacks}/\sigma_{\perp TCNQ\ stacks} \approx 2.0$ at 300 K). Hence the obtained compound is a quasi-two-dimensional semiconductor ($\rho_\perp/\rho_\parallel \approx 1.3 \times 10^3$; inset, Figure 7) in contrast to the majority of known TCNQ salts, which are generally the quasi-one-dimensional conductors.[4] The averaged value of the in-plane
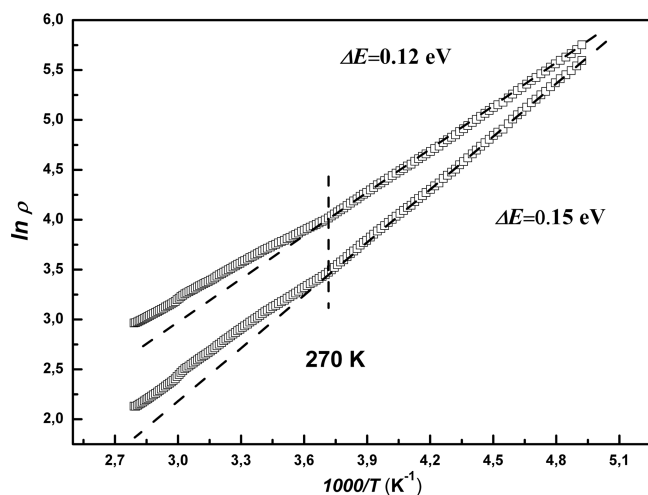
Figure 6. Temperature dependence of the in-plane (ab) resistivities measured by Montgomery method. The vertical dashed line corresponds to the temperature at which the deviation from the exponential dependence takes place.
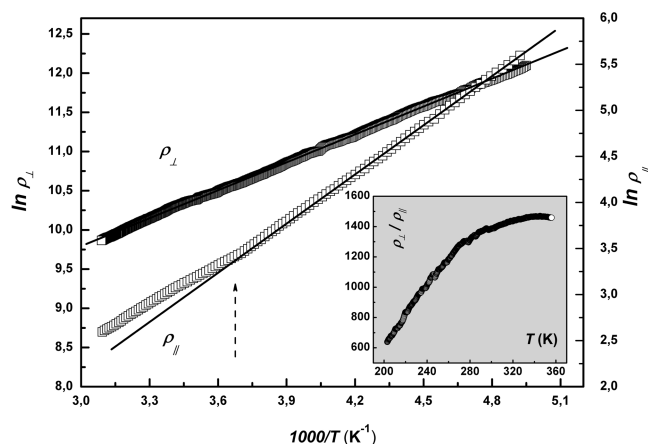

Figure 7. Temperature dependence of the in-plane and out-of-plane resistivities measured by Montgomery method. (inset) Temperature dependences of the resistivity anisotropy $\rho_\perp/\rho_\parallel$.

tively, charge densities on the $TCNQ^{\delta-}$ units in the crystals **I** ($\delta_{A,B} = -0.58$ and -0.84 at 300 K; see also Table 1) are noticeably different from the more homogeneous charge density values in ref 11a ($\delta_{A,B} = -0.63$ and -0.74 at 230 K). A peculiar feature of the crystal **I** is a quasi-two-dimensional character of conductivity due to the shortened C···N contacts between TCNQ stacks in the ab plane (Supporting Information, Figures S6 and S7). The TCNQ molecules are not directly coordinated to the Fe(II) cations in the $[Fe\{HC(pz)_3\}_2]^{2+}$ complexes. Therefore, it is unlikely that the d-orbitals of the metal ion directly interact with the π-states of the conducting electrons. However, the organic network is not completely isolated from the Fe(II) complexes in terms of cross relaxation (spin−spin interactions) due to short contacts through the ligand and dipole−dipole interactions. This channel is of interest with regard to a manipulation of the spin polarization of the delocalized charge carriers via the switchable local moments.

The bulk static magnetic susceptibility χ was measured for the polycrystalline sample in the temperature range of 2−400 K (Figure 8). Two spin ensembles contribute to the susceptibility,
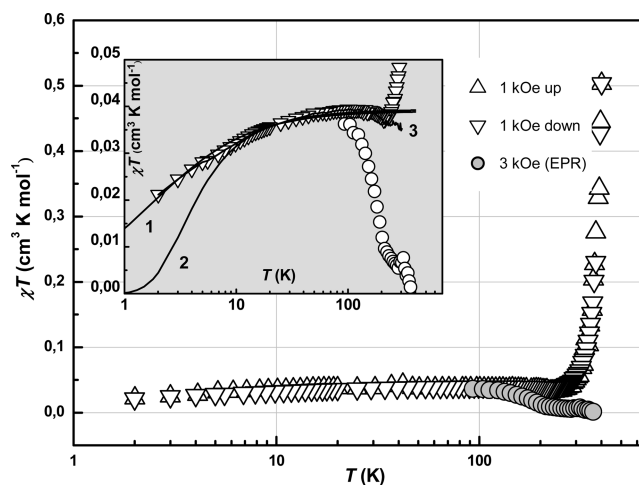

Figure 8. Temperature dependences of the product χT ($B = 1$ kOe, cooling ($\triangledown$) and heating ($\triangle$) regimes, SQUID). ($\bullet$) The product $I_{EPR}T$ measured at $B = 3$ kOe by EPR. (inset) Detailed low-temperature segment of the dependence χT. The solid line (1) is a best fit to a Curie−Weiss law with $\theta = -1.8$ K and spin concentration 2.6% ($C = 0.375$ cm^3 K mol^{-1}); solid line (2) indicates singlet−triplet model with spin gap value $J_{ST} = -7$ K and scaling factor ∼1/3. The solid line (3) represents a difference between the product χT and calculated contribution of HS Fe(II) spins.

conductivity at room temperature is $5.2 \times 10^{-2} \, \Omega^{-1} \, cm^{-1}$. With respect to the data in the Figure 5, it shows similar exponential behavior with noticeably smaller ΔE values varying between principal axes in the plane from 0.12 to 0.15 eV. A distinct deviation from the theoretical dependence takes place at $T >$ 270 K for the temperature curves of the in-plane resistivities measured along the principal axes (Figures 5 and 6). Surprisingly, this feature was not observed for the out-of-plane component of resistivity $\rho_\perp(T)$, shown in Figure 7. This is a direct indication that the transversal transport is not affected by the SCO transition.

Semiconducting behavior was expected for the trimeric dianion sublattice $[(TCNQ)_3^{2-}]_n$ because of overlapping π-orbitals of the TCNQ molecules within the trimer and increased intertrimer distances 3.36 Å (Figure 3). The conductivity at room temperature for our crystals is an order of magnitude smaller than that reported for two other conducting SCO complexes.[11a] This difference is associated with the structure of the TCNQ stacks. In **I**, the stacks are subdivided into the pronounced triads, while in the other structures the stacks have more regular periodicity. Respec-

namely, the localized moments of Fe(II) and TCNQ spin system. Below 300 K, the known complexes $[Fe\{HC(pz)_3\}_2]^{2+}$ with inorganic diamagnetic counterions exist in the LS state.[5c,13] As was shown in a structure characterization section the octahedral coordination site FeN$_6$ at 100 K facilitates a nonmagnetic ground state with the electronic configuration $t_{2g}^6 e_g^0$ and S = 0 (LS) for all the Fe(II) cations in the crystal. A reversible SCO $^1A_1 \leftrightarrow ^5T_2$ usually takes place above 300 K for similar known cationic complexes.[5c,13] Hence, a weak magnetic response below 270 K, presented in terms of the product χT (Figure 8), is related to the TCNQ spin system. Above 270 K the χT value dramatically increases; that is, the $[Fe\{HC-(pz)_3\}_2]^{2+}$ complexes undergo SCO transition (inset, Figure 8). A fully realized HS state was not achieved, because it rests above the stability threshold for this structure. The

thermogravimetric analysis indicates that the structure remains stable up to 450 K (Figure S1). We applied a symmetric Boltzmann distribution model to estimate a midpoint of the transition, T^*.[16a] The g-factor was set as 2.0 according to the value of the effective magnetic moment in the refs 5c and 13d−f The magnitude boundaries for the χT fitting curve was set between the experimental level $\chi T(100\ K) = 0.035\ cm^3 \cdot K \cdot mol^{-1}$ (LS) and the estimated one $\chi T(800\ K) = 3.035\ cm^3 \cdot K \cdot mol^{-1}$ (HS, gray horizontal line in Figure 9). The boundaries

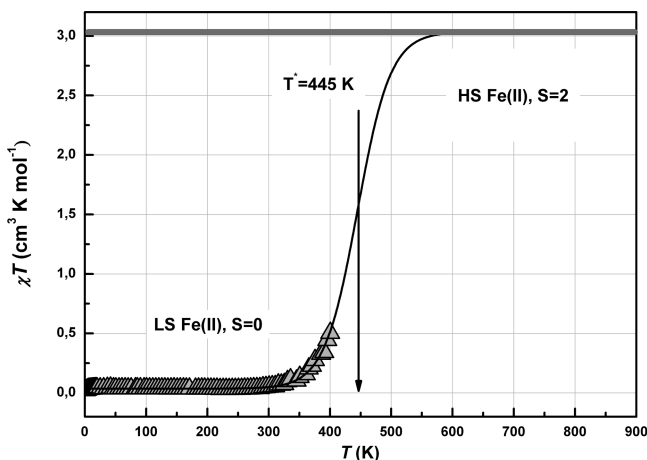**Figure 9.** SCO transition in $[Fe\{HC(pz)_3\}_2](TCNQ)_3$. (▲) Experimental χT data. Solid line is simulation by a Boltzmann distribution, $\chi T(100\ K) = 0.035\ cm^3 \cdot K \cdot mol^{-1}$, $\chi T(800\ K) = 3.035\ cm^3 \cdot K \cdot mol^{-1}$.

took into account the paramagnetic contribution from TCNQ spins below the transition and the theoretical estimate for S = 2 local moments plus the TCNQ response above it. A best-fit curve is shown in Figure 9. The SCO parameters were T^* = 445 K and $\Delta T_{1/2}$ = 200 K for the midpoint and the width of the transition. This result correlates well with the X-ray analysis, where ∼50% of Fe(II) centers in HS state were detected at 450 K. The behavior of χT at heating and cooling regimes of the measurements was reversible up to 400 K, indicating absence of significant cooperative effects. As the Fe(II) cations were supposed to have a zero magnetic moment below 270 K the total magnetic response should have been attributed to the local and/or delocalized spin moments S = 1/2 of the TCNQ sublattice. Indeed, if the low-temperature magnetic response arises due to the residual Fe(II) cations in HS configuration (S = 2 defects), then the respective magnetization curve, $M(B)$ (Figure 10), must follow a Brillouin function for S = 2 (dashed line). However, that did not happen. Best-fit curves were obtained for S = 1/2 with a scaling factor k = 0.067, which corresponded to ∼7% concentration of the electronic spins (dotted line), or ∼2% spin pairs with weak anti-ferromagnetic (AFM) interactions (solid line in Figure 10). A detailed analysis of the $M(B)$ and χT data presented in the Supporting Information confirms that the contribution of Fe(II) magnetic moments at the temperatures below 270 K is negligible.

The temperature evolution of χT below 300 K was described by two different models: weakly interacting local moments (defects with S = 1/2) and singlet−triplet spin excitations in S = 1/2 dimerized spin chain.[16b] The fitting curves are shown in the inset to Figure 8 in the logarithmic temperature scale. The Curie−Weiss approximation with $\theta = -1.8$ K and spin concentration 2.6% ($C = 0.375\ cm^3\ K\ mol^{-1}$) described well

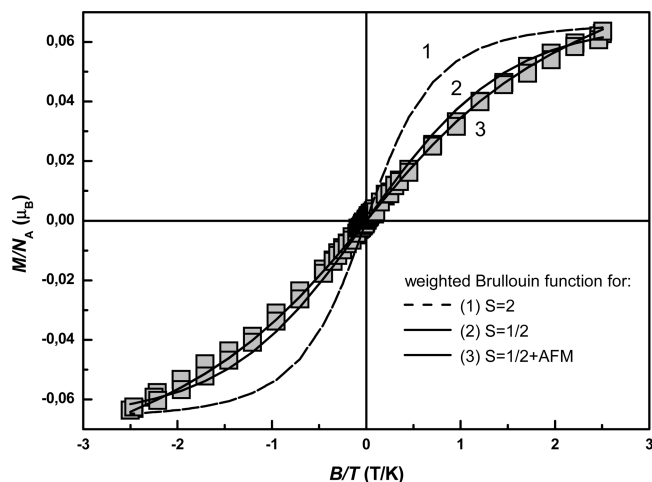**Figure 10.** Field dependence of the magnetization, $M(B)$, measured at T = 2.0 K. Lines denote the weighted Brillouin functions for S = 2 (dashed line, 1) and for two spins S = 1/2 on the TCNQ triad (solid lines, 2 and 3) with scaling factors $k_2 = 1.6 \times 10^{-2}$ and $k_3 = 3.4 \times 10^{-2}$, respectively. The fitting line 2 takes into account weak AFM interactions.

the experimental data points over the entire temperature range without temperature-independent paramagnetic (TIP) contribution[16c] (for the details on the Curie and TIP components see Supporting Information). In the meantime, this result does not seem realistic, because ∼3% of randomly distributed paramagnetic defects ($TCNQ^{\bullet-}$ radicals) will not be able to interact anti-ferromagnetically. Singlet−triplet model with the spin gap value $J_{ST} = -7$ K and scaling factor ∼1/3 also fitted well to the experiment. We believe that the model of thermally activated spin states in the TCNQ layers gives a realistic scenario for our system. The scaling factor arises due to a quasi-two-dimensional character of the electronic structure of the TCNQ sublattice, revealing itself in the experiment with polycrystals. Spectral anisotropy as well as a zero-field splitting might be also a reason for some difference between theory and experiment below 8 K (see Supporting Information).[16d]

The liquid nitrogen EPR spectrum of the polycrystalline sample is an intensive signal with the axial anisotropy of g-factor, $\Delta g = 3 \times 10^{-4}$. A central component with $g_{\parallel} = 2.005(1)$ has a Lorentzian line shape (Supporting Information, Figures S10 and S11). The line shape of the central component was reconstructed from the high-field half of the first derivative signal. The Figure S10 shows a comparison of the reconstructed EPR line with Lorentzian and Gaussian lines, which unambiguously indicate homogeneous mechanisms of broadening in the range of SCO (93−353 K). This speaks in favor of either motional narrowing or cross relaxation mechanisms rather than the supposed inhomogeneous mechanisms due to distribution of local spin−lattice relaxation times near the HS complexes. A peak-to-peak line width of the total spectrum at 93 K is ΔB_{tot} = 2.2 Oe, whereas for the $g_{\parallel}$ component it is ΔB = 1.6 Oe. At 283 K the entire spectrum narrows to a single symmetric line with $\Delta B(283\ K)$ = 1.7 Oe (Supporting Information, Figure S11). Comparison of the partial and total line width evolution while heating from 93 to 285 K (Figure 11) indicates that narrowing of the total signal is a result of isotropization of the g-tensor. It goes along with the decline of the anisotropy, $\rho_{\perp}/\rho_{\parallel}$, shown in the inset to Figure 7, and gradual evolution of the charge density in Figure 4. Spin-
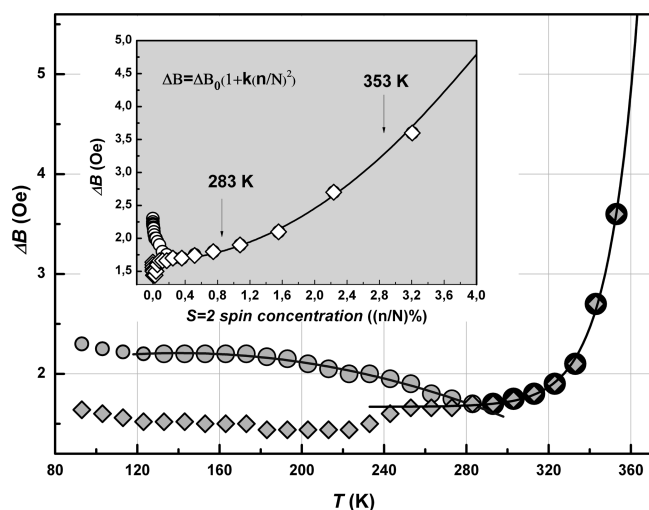
Figure 11. Temperature dependence of the EPR line width, $\Delta B(T)$: (●) peak-to-peak line width of the total EPR spectrum; (◆) peak-to-peak line width of the $g_\parallel$ component. Solid line for gray circles is a polynomial fit (narrowing); for black circles it is an exponential fit (broadening). (inset) EPR line width, $\Delta B(T)$, vs concentration of the local moments S = 2 in the cation sublattice, $n/N(\%)$.

phonon interactions usually broaden the signal with the temperature.[17a] Cross relaxation and/or fast (compare to T_2 relaxation time) translational motion of spins in conducting samples lead to the opposite.[17b,c] However, a double integrated intensity of the EPR signal, I_{EPR}, does not depend on the relaxation. Its value depends on the actual spin concentration. In the interval 93−300 K I_{EPR} decreases with the temperature from 2.16×10^{-3} at 93 K to 1.21×10^{-4} cm³ mol⁻¹, which is faster than the Curie trend (see the inset to Figure 8). As soon as the integral intensity of the absorption signal is proportional to the spin susceptibility, the product $I_{EPR}T$ was plotted in the Figure 8 in the same scale as the χT. In the vicinity of 100 K the absolute values of I_{EPR} and χ were close within 20%. This attributes the total static spin response at low temperatures and EPR signal to the same group of spin moments in the TCNQ sublattice. The EPR signal from the local moments of HS Fe(II) has not been detected. This is understandable in terms of relatively low concentration (~4% at 360 K) and fast relaxation. In turn, a high relaxation rate in the S = 2 spin reservoir provides the effective cross relaxation channel for the unpaired electron spins in the conducting layers.

Above 270 K the width of the TCNQ signal increased exponentially (Figure 11). This correlates with the appearance of the local magnetic moments in the cation sublattice as well as with the structural defects (distorted TCNQ triads) induced by the changed geometry of the individual HS Fe(II) complexes. Because of the thermal activation mechanism the concentrations of the S = 2 moments as well as the defects follow similar exponential trend. However, the magnitude factors are different: the defect concentration reaches its maximum at $T^* = 445$ K, while the concentration of the local moments saturates at $(T^* + \Delta T_{1/2}/2) = 545$ K. As soon as stability threshold was close to the T^* value we were not able to distinguish the magnetic contributions from the above sources. It is worth to say, that X-ray analysis at 450 K did not show a disorder but a sharp rearrangement of the TCNQ stacks. Thus, the local moments of the HS Fe(II) ions are more likely a source of the EPR line broadening. For various low-dimensional organic

conductors the value of the EPR line width usually weakly depends on the crystal quality, and to a certain degree it also weakly depends on the external disorder.[16e] For a random spatial distribution of the defects one could rather expect the inhomogeneous broadening mechanism than a systematic change of the spin−lattice relaxation rate due to continuous evolution of the electronic spectrum of the TCNQ structure. However, the line shape remains Lorentzian within the studied SCO range. The inset of Figure 11 demonstrates the evolution of the line width versus the concentration of the local moments S = 2 in the cation sublattice. The value of the relative concentration, $n/N(\%)$, was extracted from the magnetic susceptibility data on Figure 7. In the SCO range the line width was proportional to the squared concentration, $\Delta B = \Delta B_0(1 + k(n/N)^2)$, where $\Delta B_0 = 1.7$ Oe and $k = 1.15 \times 10^{-1}$ Oe. Surprisingly, the resistivity reveals a weaker sensitivity to the SCO. A value of relative deviation for the a- and b-components of the in-plane resistivity, $\Delta_\rho(\%) = (\rho_\parallel(T) - \rho_{\parallel calc}(T))/\rho_{\parallel calc}(T)$, shown in Figure 12, was found to reveal a
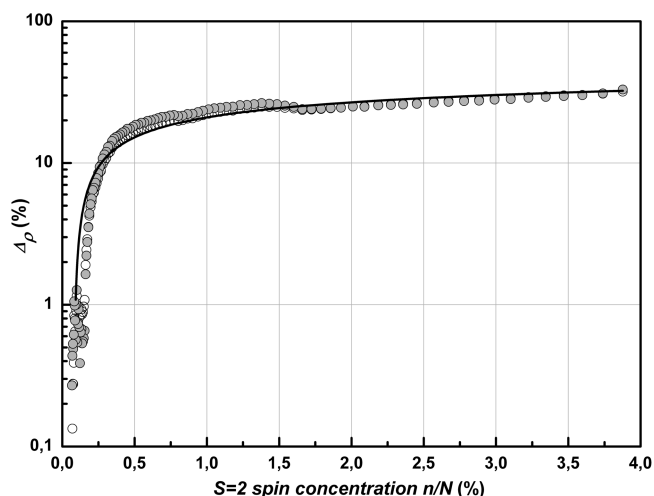

Figure 12. A relative deviation for the a- and b- components of the in-plane resistivity, $\Delta_\rho(\%) = (\rho_\parallel(T) - \rho_{\parallel calc}(T))/\rho_{\parallel calc}(T)$, vs the concentration of S = 2 local moments in the range of the SCO transition. The $\rho_{\parallel calc}(T)$ values were obtained from the a- and b- best fit curves extended to the higher temperatures (dashed lines in Figure 6). A solid line is the best fit logarithmic curve, $\Delta_\rho(\%) = A + B \times \ln(n/N)$, where $A = 0.60$ and $B = 8.51 \times 10^{-2}$. Here the $n/N(\%)$ values were extracted from the modeling curve in Figure 9.

universal logarithmic dependence on the concentration n/N, $\Delta_\rho(\%) = A + B \times \ln(n/N)$, where $A = 0.60$ and $B = 8.51 \times 10^{-2}$. Here the $\rho_{\parallel calc}(T)$ values were extracted from the a- and b- best-fit curves extended to the higher temperatures (dashed lines in Figure 6). The transverse transport, $\rho_\perp(T)$, did not react to the changes in the cation layers and therefore did not contribute to the line-broadening effect. Qualitatively this means that the probability of Zeeman spin transitions grows faster than the in-plane scattering rate (or in-plane hopping rate) of the charge carriers; that is, phenomenological Elliott or Weger approaches are not applicable.[18] This discrepancy could be explained by the activation of additional spin-relaxation channel related to the expanding reservoir of local moments in $[Fe\{HC(pz)_3\}_2]^{2+}$ complexes. A cross relaxation due to spin−spin interactions between the two spin reservoirs (i.e., local moments of Fe(II) ions in HS state and delocalized spin moments of the conduction electrons) is likely to contribute to

Table 2. Crystal Structure and Refinement Data[a] for I

temperature (K)	100	300	400	450
cell setting	triclinic	triclinic	triclinic	triclinic
space group, Z	$P\bar{1}$, 1	$P\bar{1}$, 1	$P\bar{1}$, 1	$P\bar{1}$, 1
a (Å)	8.1253(13)	8.1625(1)	8.1878(3)	8.1933(4)
b (Å)	10.0214(16)	10.1192(2)	10.2235(5)	10.2948(5)
c (Å)	16.747(3)	16.7712(2)	16.8524(6)	16.9627(4)
α (deg)	100.977(3)	101.687(1)	102.158(4)	102.726(3)
β (deg)	91.048(3)	91.046(1)	91.242(3)	91.631(3)
γ (deg)	111.167(3)	110.879(2)	110.652(4)	110.391(4)
cell volume (Å^3)	1242.7(3)	1261.26(4)	1283.3(1)	1299.48(9)
ρ (g/cm^3)	1.466	1.444	1.419	1.402
μ, cm^{-1}	3.72	3.67	3.60	3.56
refls collected/unique	11 053/6509	27 919/8585	27 704/8617	28 566/8807
R_{int}	0.0291	0.0267	0.0272	0.0239
θ_{max} (deg)	29.0	30.5	30.5	30.5
refls with $[I > 2\sigma(I)]$	4941	6867	6396	5974
parameters refined	367	367	367	367
final R_1, wR_2 $[I > 2\sigma(I)]$	0.0452, 0.1231	0.0424, 0.1110	0.0484, 0.1257	0.0502, 0.1274
goodness-of-fit	1.027	1.053	1.048	1.020
CCDC reference	1033050	1487395	1487396	1487397

[a]$C_{20}H_{20}FeN_{12} \cdot 3C_{12}H_4N_4$, FW = 1096.91, $F(000)$ = 562, λ(Mo Kα) = 0.710 73 Å.

the EPR line broadening in the SCO range but does not affect the resistivity. Even weak interactions via short contacts are able to provide an efficient relaxation channel (reciprocal bottleneck effect).[19] At present one cannot determine whether the dipole–dipole or weak superexchange interactions facilitate the cross relaxation in [Fe{HC(pz)$_3$}$_2$](TCNQ)$_3$. The important consequence is that the local magnetic moments in the Fe(II) complexes not just coexist but affect the spin degrees of freedom in the conducting TCNQ layers. In a sense, the SCO transition triggers a synergy of the two subsystems.

CONCLUSION

We prepared and structurally characterized at 100, 300, 400, and 450 K a conducting SCO compound based on Fe(II) cation complex with the electroactive trimeric dianionic TCNQ network in a fractional reduction state, [Fe{HC(pz)$_3$}$_2$]-(TCNQ)$_3$. Two crystallographically independent TCNQ species are found in the different charge states (**A**) and (**B**) forming asymmetric units in the pattern···**ABA**···**ABA**··· . The interplanar distances at 100 K are 3.04 Å inside **ABA** triads and 3.36 Å between the triads. The Fe(II) ion in [Fe{HC(pz)$_3$}$_2$] complex is in an LS state, S = 0, below 270 K, as confirmed by the average Fe–N bond length (1.968(5) Å) and magnetic measurements. A transformation to HS state begins above 270 K and reaches the midpoint of the transition at T^* = 445 K, which is confirmed by magnetic data and X-ray analysis. A fully realized HS state was not achieved, because it rests above the stability threshold (∼470 K). The transition is accompanied by equalization of interplanar spacing between the TCNQ units that is likely to facilitate the electron delocalization in TCNQ system. The conductivity along the stacks is 0.015 Ω^{-1} cm^{-1} at room temperature, and the energy gap is 0.17 eV. The shortened C···N contacts between the stacks gives rise to a quasi-two-dimensional character of conductivity in the ab plane.

A robust broadening of the TCNQ EPR signal and a pronounced deviation of the in-plane resistivity out of the exponential law are induced by the reversible SCO. The enhancement of spin relaxation triggered by the SCO transition is interpreted in terms of cross relaxation between the two spin

reservoirs: local moments of Fe(II) ions and delocalized spin moments of the conduction electrons. The [Fe{HC(pz)$_3$}$_2$]-(TCNQ)$_3$ compound is only the second example of the conducting SCO systems that combine Fe(II) SCO cation complexes with partially charged TCNQ$^{\bullet \delta -}$ radical anions in the same crystal lattice. Reasoning from the synthetic strategy used in the work, one may expect that a variety of conducting compounds comprising Fe(II) SCO complexes may be significantly expanded.

■ EXPERIMENTAL SECTION

Synthesis of [Fe{HC(pz)$_3$}$_2$](TCNQ)$_3$ (I). The crystals of **I** were obtained in argon atmosphere by mixing the boiling solutions [Fe{HC(pz)$_3$}$_2$]I$_2$ H$_2$O (0.13 mmol) in 30 mL of MeOH/absoluteEtOH/MeCN (1:1:1) and TCNQ (0.26 mmol) in MeCN (10 mL) followed by slow cooling of the resulting solution. After 2 d, black shining crystals in the shape of hexagons were formed. The crystals were collected by filtration, washed with ethanol and ether, and dried under vacuum at room temperature. Yield: 75%. Anal. Calcd (Found) for **I** (C$_{56}$H$_{32}$N$_{24}$Fe): C, 61.32 (61.38); H, 2.94 (3.15); N, 30.65 (30.30)%. It is worth to note that the same crystals were formed at the ratios of starting reagents of 1:3 and 1:4. Also note that a hexagon shape of the obtained crystals (Supporting Information, Figure S9) is not typical for TCNQ salts, which generally have a needlelike shape.

Thermogravimetric Analysis. The thermogravimetric analysis was performed in argon atmosphere with a heating rate of 5.0 °C min^{-1} using a NETZSCH STA 409 C Luxx thermal analyzer, interfaced to a QMS 403 Aelos mass spectrometer, which allows simultaneous thermogravimetry, DSC, and mass-spectrometry measurements.

X-ray Crystallography. X-ray single-crystal diffraction experiments were performed with a Bruker SMART APEX2 CCD diffractometer at 100 K and an Oxford Diffraction Gemini-R CCD diffractometer at 300, 400, and 450 K [λ(Mo Kα) = 0.710 73 Å, ω-scans]. The structures were solved by direct method and refined by a full-matrix least-squares technique against F^2 in an anisotropic approximation for all non-hydrogen atoms. Hydrogen atoms were located from the Fourier synthesis of the electron density and refined in the isotropic approximation. All calculations were made using SHELXTL PLUS 5.0 (for the 100 K structure) and the SHELX-97 programs.[20] The main structural and refinement parameters are listed

in Table 2. X-ray powder diffraction pattern was collected on a Siemens D500 powder diffractometer with Bragg−Brentano geometry using Cu Kα1 radiation (1.540 56 Å). Additional crystallographic information is available in the Supporting Information.

Transport and Magnetic Measurements. The dc resistivity measurements were performed on single crystals by a standard four-probe method with the current flow parallel to the TCNQ stacks in the temperature range of 120−360 K. We were restricted in the heating limit, because the higher temperature was dangerous for our equipment. Four annealed platinum wires (0.02 mm in diameter) were attached to a crystal surface by a graphite paste (Supporting Information, Figure S9). The applied current was in the limits of 10−100 nA. This geometry is convenient for the test measurements to reveal the features in the temperature dependences of the resistance, but in the strongly anisotropic sample the measured value includes the mixture of both in-plane and out-of-plane components of the resistivity tensor, because the current is distributed nonuniformly through the sample cross section. This is why in the control experiments we measured the resistivity tensor components separately. To measure in-plane anisotropy we used Montgomery method[21] on the samples, which had the shape of the thin hexagon plates elongated in the direction of TCNQ stacks (the typical sample shape is shown in the Supporting Information, Figure S9). So, using two pairs of contacts attached to the plate corners on the long sides of the plate we could measure two components of the resistivity tensor along and perpendicular to the TCNQ stacks. To measure the out-of-plane resistivity tensor we used the modified Montgomery method[22] on the sample with two pairs of contacts attached to the opposite sample surfaces.

Magnetic measurements were performed by using a Quantum Design MPMS-5-XL SQUID magnetometer. The static magnetic susceptibility $\chi(T)$ of the polycrystalline sample was measured at the magnetic field B = 0.1 T, at cooling and heating regimes in the temperature range of 2−400 K. Field dependences of the magnetization $M(B)$ were obtained at 2.0 K in the field range from −5.0 to +5.0 T. The sample had been cooled to 2.0 K in a weak magnetic field B = 0.1 T. Then the measurements were performed at increasing field to 5.0 T and further field decreasing with a sign reversal to −5.0 T.

EPR spectra were recorded in the temperature range of 90−350 K on a standard homodyne X-band Bruker Elexsys E580 FT/CW X-Band spectrometer (9.4 GHz). The temperature was set and stabilized at a rate of 1−2 K min^{-1} with an accuracy of 0.1 K using a liquid nitrogen gas-flow cryostat. The spin contribution to the magnetic susceptibility was determined by the double integration of the EPR signal (Schumacher−Slichter method) under conditions for the field sweep $\delta B_{sw} \geq 10\Delta B$ (ΔB is the peak-to-peak EPR line width). In this case, the error of the method for the Lorentz-type EPR signal is ∼10%. The pyrolytic coal product with g = 2.002 83 was used as the standard of a spin concentration.

ASSOCIATED CONTENT

⑤ Supporting Information

The Supporting Information is available free of charge on the ACS Publications website at DOI: 10.1021/acs.inorgchem.6b01829. CCDC Nos. 1033050, 1487395, 1487396, and 1487397 contain supplementary crystallographic data for this paper. These data can be obtained free of charge from the Cambridge Crystallographic Data Centre via www.ccdc.cam.ac.uk/data_request/cif.

Crystallographic CIF file CCDC 1033050 (CIF)

Crystallographic CIF file CCDC 1487395 (CIF)

Crystallographic CIF file CCDC 1487396 (CIF)

Crystallographic CIF file CCDC 1487397 (CIF)

Thermogravimetric data, various structural figures, tabulated bond lengths and angles, additional EPR data, photo of a crystal with contacts for measurement of conductivity, discussion of magnetic response at low temperatures and below the SCO transition (PDF)

AUTHOR INFORMATION

Corresponding Authors
*E-mail: yuri.shvachko@gmail.com.
*E-mail: starichenko@imp.uran.ru.
*E-mail: yagubski@icp.ac.ru.

Author Contributions
All authors have given approval to the final version of the manuscript.

Notes
The authors declare no competing financial interest.

REFERENCES

(1) (a) *Multifunctional Molecular Materials*; Ouahab, L., Ed.; Pan Stanford Publishing Pte. Ltd: Singapore, 2013. (b) Coronado, E.; Day, P. *Chem. Rev.* **2004**, *104*, 5419−544. (c) Kobayashi, H.; Cui, H.; Kobayashi, A. *Chem. Rev.* **2004**, *104*, 5265−5288. (d) Enoki, T.; Miyazaki, A. *Chem. Rev.* **2004**, *104*, 5449−5477. (e) Kushch, N. D.; Yagubskii, E. B.; Kartsovnik, M. V.; Buravov, L. I.; Dubrovskii, A. D.; Biberacher, W.; et al. *J. Am. Chem. Soc.* **2008**, *130*, 7238−7240. (f) Vyaselev, O. M.; Kartsovnik, M. V.; Biberacher, W.; Zorina, L. V.; Kushch, N. D.; Yagubskii, E. B. *Phys. Rev. B: Condens. Matter Mater. Phys.* **2011**, *83*, 094425−6.

(2) (a) Valade, L.; Malfant, I.; Faulmann, C. In *Multifunctional Molecular Materials*; Ouahab, L., Ed.; Pan Stanford Publishing Pte. Ltd: Singapore, 2013, 163−174. (b) Sato, O.; Li, Z.-Y.; Yao, Z.-S.; Kang, S.; Kanegawa, S. In *Spin-Crossover Materials: Properties and Applications*; Halcrow, M. A., Ed.; John Wiley & Sons: Oxford, U.K, 2013, 304−319.

(3) (a) Cassoux, P. *Coord. Chem. Rev.* **1999**, *185*, 213−232. (b) Kato, R. *Chem. Rev.* **2004**, *104*, 5319−5346.

(4) (a) Melby, L. R.; Harder, R. J.; Hertler, W. R.; Mahler, W.; Benson, R. E.; Mochel, W. E. *J. Am. Chem. Soc.* **1962**, *84*, 3374−3387. (b) Shchegolev, I. F. *Phys. Status Solidi (a)* **1972**, *12*, 9−45. (c) Shibaeva, R. P.; Atovmyan, L. O. *J. Struct. Chem.* **1972**, *13*, 514−531. (d) Yagubskii, E. B. In *Organic Conductor, Superconductors, and Magnets: From Synthesis to Molecular Electronics*; Ouahab, L., Yagubskii, E. B., Eds.; Kluwer Academic Publishers: Dordrecht, Netherlands, 2003, 45−65. (e) Kojima, H.; Zhang, Z.; Dunbar, K. R.; Mori, T. *J. Mater. Chem. C* **2013**, *1*, 1781−1790. (f) Kubota, H.; Takahashi, Y.; Harada, J.; Inabe, T. *Cryst. Growth Des.* **2014**, *14*, 5575−5584.

(5) (a) *Spin-Crossover Materials: Properties and Applications*; Halcrow, M. A., Ed.; John Wiley & Sons: Oxford, U.K, 2013. (b) Halcrow, M. A. *Chem. Soc. Rev.* **2011**, *40*, 4119−4142. (c) Lavrenova, L. G.; Shakirova, O. G. *Eur. J. Inorg. Chem.* **2013**, *2013*, 670−682.

(6) Murata, K.; Kagoshima, S.; Yasuzuka, S.; Yoshino, H.; Kondo, R. *J. Phys. Soc. Jpn.* **2006**, *75*, 051015.

(7) (a) Dorbes, S.; Valade, L.; Real, J. A.; Faulmann, S. *Chem. Commun.* **2005**, 69−71. (b) Faulmann, C.; Dorbes, S.; Real, J. A.; Valade, L. *J. Low Temp. Phys.* **2007**, *142*, 265−270. (c) Faulmann, C.; Dorbes, S.; Garreau de Bonneval, B.; Molnar, G.; Bousseksou, A.; Gomez-Garcia, C. J.; Coronado, E.; Valade, L. *Eur. J. Inorg. Chem.* **2005**, *2005*, 3261−3270. (d) Faulmann, C.; Jacob, K.; Dorbes, S.; Lampert, S.; Malfant, I.; Doublet, M.-L.; Valade, L.; Real, J. A. *Inorg. Chem.* **2007**, *46*, 8548−8559. (e) Takahashi, K.; Cui, H.-B.; Okano, Y.;

Kobayashi, H.; Einaga, Y.; Sato, O. *Inorg. Chem.* **2006**, *45*, 5739−5741. (f) Takahashi, K.; Cui, H.-B.; Okano, Y.; Kobayashi, H.; Mori, H.; Tajima, H.; Einaga, Y.; Sato, O. *J. Am. Chem. Soc.* **2008**, *130*, 6688−6689. (g) Fukuroi, K.; Takahashi, K.; Mochida, T.; Sakurai, T.; Ohta, H.; Yamamoto, T.; Einaga, Y.; Mori, H. *Angew. Chem., Int. Ed.* **2014**, *53*, 1983−1986.

(8) Nakano, M.; Fujita, N.; Matsubayashi, G. E.; Mori, W. *Mol. Cryst. Liq. Cryst.* **2002**, *379*, 365−370.

(9) Nihei, M.; Takahashi, N.; Nishikawa, H.; Oshio, H. *Dalton Trans.* **2011**, *40*, 2154−2156.

(10) (a) Kunkeler, P. J.; van Koningsbruggen, P. J.; Cornelissen, J. P.; van der Horst, A. N.; van der Kraan, A. M.; Spek, A. L.; Haasnoot, J. G.; Reedijk, J. *J. Am. Chem. Soc.* **1996**, *118*, 2190−2197. (b) Cornelissen, J. P.; van Diemen, J. H.; Groeneveld, L. R.; Haasnoot, J. G.; Spek, A. L.; Reedijk, J. *Inorg. Chem.* **1992**, *31*, 198−202.

(11) (a) Phan, H.; Benjamin, S. M.; Steven, E.; Brooks, J. S.; Shatruk, M. *Angew. Chem., Int. Ed.* **2015**, *54*, 823−827. (b) Zhang, X.; Xie, H.; Ballesteros-Rivas, M.; Wang, Z.-X.; Dunbar, K. R. *J. Mater. Chem. C* **2015**, *3*, 9292−9298. (c) Zhang, X.; Wang, Z.-X.; Xie, H.; Li, M.-X.; Woods, T. J.; Dunbar, K. R. *Chem. Sci.* **2016**, *7*, 1569−1574.

(12) Shakirova, O. G.; Lavrenova, L. G.; Kuratieva, N. V.; Naumov, D.; Daletsky, V. A.; Sheludyakova, L. A.; Logvinenko, V. A.; Vasilevsky, S. F. *Russ. J. Coord. Chem.* **2010**, *36*, 275−283 (English translation)..

(13) (a) Anderson, P. A.; Astley, T.; Hitchman, M. A.; Keene, F. R.; Moubaraki, B.; Murray, K. S.; Skelton, B. W.; Tiekink, E. R. T.; Toftlund, H.; White, A. H. *J. Chem. Soc., Dalton Trans.* **2000**, 3505−3512. (b) Reger, D. L.; Little, Ch.A.; Rheingold, A. L.; Lam, M.; Liable-Sands, L. M.; Rhagitan, B.; Concolino, T.; Mohan, A.; Long, G. J.; Briois, V.; Grandjean, F. *Inorg. Chem.* **2001**, *40*, 1508−1520. (c) Reger, D. L.; Little, Ch.A.; Young, V. G.; Pink, M. *Inorg. Chem.* **2001**, *40*, 2870−2874. (d) Reger, D. L.; Little, Ch.A.; Smith, M. D.; Rheingold, A. L.; Lam, K-Ch.; Concolino, T. L.; Long, G. J.; Hermann, R. P.; Grandjean, F. *Eur. J. Inorg. Chem.* **2002**, *2002*, 1190−1197. (e) Shakirova, O. G.; Lavrenova, L. G.; Daletsky, V. A.; Shusharina, E. A.; Griaznova, T. P.; Katsyuba, S. A.; Syakaev, V. V.; Skripacheva, V. V.; Mustafina, A. R.; Solovieva, S. E. *Inorg. Chim. Acta* **2010**, *363*, 4059−4064. (f) Shakirova, O. G.; Daletsky, V. A.; Lavrenova, L. G.; Trubina, S. V.; Erenburg, S. B.; Zhizhin, K.Yu.; Kuzhetsov, T. N. *Russ. J. Inorg. Chem.* **2013**, *58*, 650−656.

(14) (a) Flandrois, S.; Chasseau, D. *Acta Crystallogr., Sect. B: Struct. Crystallogr. Cryst. Chem.* **1977**, *33*, 2744−2750. (b) Kistenmacher, T. J.; Emge, T. J.; Bloch, A. N.; Cowan, D. O. *Acta Crystallogr., Sect. B: Struct. Crystallogr. Cryst. Chem.* **1982**, *38*, 1193−1199. (c) Ballesteros-Rivas, M.; Ota, A.; Reinheimer, E.; Prosvirin, A.; Valdes-Martinez, J.; Dunbar, K. R. *Angew. Chem.* **2011**, *123*, 9877−9881. (d) Zhang, X.; Zhang, Zh.; Zhao, H.; Mao, J.-G.; Dunbar, K. R. *Chem. Commun.* **2014**, *50*, 1429−1431.

(15) Bigoli, F.; Deplano, P.; Devillanova, F. A.; Girlando, A.; Lippolis, V.; Mercuri, M.-L.; Pellinghelli, M.-A.; Trogu, E. F. *J. Mater. Chem.* **1998**, *8*, 1145−1150.

(16) (a) Kahn, O. *Molecular Magnetism*; Wiley-VCH: New York, 1993. (b) Bellec, N.; Lorcy, D.; Boubekeur, K.; Carlier, R.; Tallec, A.; Los, Sz.; Pukacki, W.; Trybula, M.; Piekara-Sady, L.; Robert, A. *Chem. Mater.* **1999**, *11*, 3147−3153. (c) Ballester, L.; Gil, A. M.; Gutierrez, A.; Perpinan, M. F.; Azcondo, M. T.; Sanchez, A. E.; Coronado, E.; Gomez-Garcıa, C. J. *Inorg. Chem.* **2000**, *39*, 2837−2842. (d) Kulikov, A. V. In *Aspects on Fundaments and Applications of Conducting Polymers Publisher*; Motheo, A., Ed.; InTech, 2012. (e) Williams, J. M.; Ferraro, J. R.; Thorn, R. J.; Carlson, K. D.; Geiser, U.; Wang, H. H.; Kini, A. M.; Whangbo, M.-H. *Organic Superconductors, Synthesis, Structure, Properties and Theory*; Prentice Hall: Englewood Cliffs, NJ, 1992.

(17) (a) Poole, Ch. P., Jr.; Farach, H. A. *Handbook of Electron Spin Resonance*; Springer Science & Business Media, 1999; Vol. 2. (b) Krinichnyi, V. I. *2-mm Wave Band EPR Spectroscopy of Condensed Systems*; CRC Press, Inc: 1995; Chapter 4. (c) Poole, Ch. P., Jr.; Farach, H. A. *Relaxation in Magnetic Resonance: Dielectric and Mossbauer Applications*; Elsevier Inc, 1971.

(18) *The Physics and Chemistry of Low-Dimensional Solids*; Alcácer, L., Ed.; NATO Advance Study Institutes Series, 1980.

(19) Barnes, S. E. *Adv. Phys.* **1981**, *30*, 801−938.

(20) Sheldrick, G. M. *Acta Crystallogr., Sect. A: Found. Crystallogr.* **2008**, *64*, 112−122.

(21) Montgomery, H. C. *J. Appl. Phys.* **1971**, *42*, 2971.

(22) Buravov, L. I. *Sov. Phys. Technol. Phys.* **1989**, *34*, 464.